Heliyon 9 (2023) e15195

Contents lists available at ScienceDirect

Heliyon

journal homepage: www.cell.com/heliyon

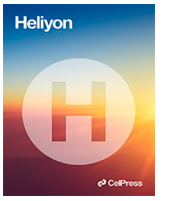

Review article

Robust electrical impedance tomography for biological application: A mini review

Yang Li [a], Nan Wang [a], Li-Feng Fan [b], Peng-Fei Zhao [c], Jin-Hai Li [d], Lan Huang [a], Zhong-Yi Wang [a,*]

[a] College of Information and Electrical Engineering, China Agricultural University, China
[b] School of Electronics, Peking University, China
[c] China Electronics Standardization Institute, China
[d] School of Mechanical Engineering, Ningxia University, China

ARTICLE INFO

Keywords:
Electrical impedance tomography
Hardware design
Biological tissue
Machine learning

ABSTRACT

Electrical impedance tomography (EIT) has been used by researchers across several areas because of its low-cost and no-radiation properties. Researchers use complex conductivity in bio-impedance experiments to evaluate changes in various indicators within the image target. The diverse volumes and edges of biological tissues and the large impedance range impose dedicated demands on hardware design. The EIT hardware with a high signal-to-noise ratio (SNR), fast scanning and suitable for the impedance range of the image target is a fundamental foundation that EIT research needs to be equipped with. Understanding the characteristics of this technique and state-of-the-art design will accelerate the development of the robust system and provide a guidance for the superior performance of next-generation EIT. This review explores the hardware strategies for EIT proposed in the literature.

1. Introduction

Plant and animal body tissues are typically optically opaque and only a few microns thick when examined under a light microscope. Researchers have utilized a range of theories and methods to investigate the structure and function of plant and animal tissues and organs in situ and non-destructively. The most widely practised of these are CT and MRI. EIT technology has been adopted by researchers in a variety of areas in recent years due to its non-invasive, radiation-free, high temporal resolution, low-cost equipment, and strong biocompatibility. It can scan lung ventilation, stroke, breast tumours, and tissue culture, and even have been used as biosensor [1]. For plants, it is often used as a measurement tool to study the phenotype of the plant root system and the state of soil water content in the root zone of growth [2].

The EIT approach has been used in most research for lung ventilation, and Adler et al. established the GREIT reconstruction method using Electrical Impedance Tomography and Diffuse Optical Tomography Reconstruction Software (EIDORS) [3], which was approved by a significant consensus of a representative group of experts in the clinical application of lung monitoring. Kuen et al. found air-filled expanded lungs have lower conductivity and higher dielectric constants based on GREIT [4]. Farooq et al. added internal electrodes to the EIT system for lung ventilation monitoring to reduce the effect of insulating boundaries such as fat and bone [5]. Jang et al. confirmed the correlation of impedance data from EIT images with mechanical ventilator-induced air intake using KHU Mark 2.5 [6].

* Corresponding author.
E-mail address: wzyhl@cau.edu.cn (Z.-Y. Wang).

https://doi.org/10.1016/j.heliyon.2023.e15195
Received 31 October 2022; Received in revised form 10 March 2023; Accepted 29 March 2023
Available online 4 April 2023

Darnajou et al. developed a 16-electrode EIT system with multi-frequency excitation to increase the imaging speed to 3906 frames per second (fps) [7]. Thereafter, a 3-layer with 48 active electrodes EIT system was designed to provide 3D real-time lung images at 10 fps, i.e., 10 measurement points were acquired every second [8,9]. Tregidgo et al. used EIT to monitor lung ventilation in real-time and applied feedback signals to adjust ventilator pressure to avoid ventilator-induced lung injury [10]. Qu et al. presented the first chest EIT device (Pulmo EIT-100) for ICU in China [11].

In cerebrovascular disease and brain tumour studies, the 1% brain impedance variation in neurological function due to skull occlusion requires measurement instruments with sensitivity at 80 dB. To detect neural function in the time domain, a frame rate of 100 fps was required [12]. For this purpose, Dong et al. explored the effects of electrode material [13], excitation frequency [14], and electrode position interference [15] on brain detection. A reference electrode approach was proposed to monitor and evaluate the electrode contact condition in real time [16]. For high-resolution imaging of brain tumours, Woo et al. developed Magnetic resonance electrical impedance tomography (MREIT). The conductivity distribution was solved by calculating the current density using the current excitation of biological tissue and measuring the induced flux density using an MRI scanner [17–20].

In a smaller-scale study, Hong et al. simulated and found that more than 80 electrodes were required to reconstruct a cancer model with a volume of 0.1% of the breast model [21]. Lee et al. designed the EIT integrated circuit (IC) chip with a wide bandwidth of 10 MHz, which could detect small-sized image target objects up to 0.5 cm [22]. Lee et al. designed a breast cancer EIT system that could filter out ECG signals [23]. Cheng et al. developed a method of detecting the state of the tissue in a specific area by controlling the electrode position with a robotic arm, which can be used to automatically locate pathological tissue or lymph [24,25]. Rao et al. designed a miniaturised EIT system using application specific integrated circuit and proceeded with the EIT open domain problem for prostate cancer lesions [26,27]. EIT has also been used for tissue culture, Yang et al. found frequency difference imaging to meet the variation of conductivity of the image target with frequency. Based on this finding, they used scaffolds to immobilize cells inside the culture dish without affecting the imaging results [28,29]. The 3-D conductivity changes associated with transient cell-drug reaction processes were observed for the first time in real-time [30]. Conductivity binary images and boundary voltages were fused to solve the problem of poor EIT imaging pixels [31–33].

In recent years EIT technology has been introduced into human sensor design. Measuring the impedance changes caused by muscle and bone movements within the forearm and classifying the movements through neural networks thus controlling the prosthesis movements [34,35]. Jiang et al. further conducted a study on gesture recognition using 3D-EIT, obtaining higher image resolution and classification accuracy [36]. Russo et al. designed an artificial sensitive skin sensor using EIT [37]. Zhu et al. developed an electrical impedance tomography toolkit (EIT-kit) for health and motion sensing devices. The EIT-kit was applied to muscle monitoring for physical rehabilitation, wearable gesture recognition devices, non-invasive distracted driving detection, and visualization of biological tissues [38].

EIT has also been applied to the study of plant root phenology and soil moisture. Gnecchi et al. measured soil hydraulic conductivity in situ using EIT and dynamically imaged the infiltration process [39]. Corona-Lopez demonstrated that EIT could be applied to characterizing root structure and plant-pathogen interactions in opaque growth media [40]. Weigand observed that the magnitude of the low-frequency polarization response of the root system decreased with the physiological decline of the root system. Multi-frequency EIT was proposed as a method for monitoring and physiological (i.e., functional) characterization of crop roots [41]. Our research group monitored the dehydration of an intact maize cob in situ over 5 days and observed the changes in moisture distribution [42].

The primary issue in the EIT field is hardware design. Developing high-speed, stable EIT hardware requires an iterative process from design to application for implementing complex digital and analogue parts. Differences in EIT hardware design have emerged according to the research objectives and usage environment. Therefore, it is necessary to aim the design of EIT hardware according to the imaging target characteristics for high SNR and fast measurement. The hardware design and debugging cycle time was long and the upgrade iteration speed was slow. Therefore, it is particularly important to design the hardware system, and designing an EIT hardware device with high SNR and high bandwidth is the basis of the research work. The EIT hardware's challenges are as follows: 1) the output impedance of the current source 2) the contact impedance of the electrodes and the measurement target 3) the circuit board's and cables' dispersed capacitance 4) the voltmeter's adaptive amplification 5) the rate of measuring.

This paper provides an overview of the principles and hardware circuit design of EIT imaging for bioimpedance (including plants and animals) studies. The emphasis is on the existing EIT modular design scheme, error causes and correction or compensation. Section II briefly describes the bioimpedance conductivity characteristics and electrical impedance imaging principles. Section III reviews existing modular EIT design and discusses how to design hardware circuits with high SNR. Section IV discusses the remaining challenges in EIT hardware circuit design. Concluding remarks are drawn in Section V.

2. Research methodology

This review collates hardware design developments of EIT for bioimpedance detection and briefly summarises cutting edge advances in machine learning combined with EIT. Summarises the technical problems encountered by other academics in EIT hardware design and the solutions provided.

2.1. Data sources

All these resources were sourced from widely used search platforms including Google Scholar, web of science, EI Compendex, MEDLINE and PubMed. These databases are reputable bibliographic sources.

2.2. Search procedure

In order to ensure appropriate primary search terms are used and relevant papers are carefully selected for the review purpose, the literature search method of Kitchenham et al. [43] was adopted. The topics, keywords, abstracts and full text content of these publications were searched to select those closely related to the topic of interest for further analysis. Search terms include: electrical impedance tomography, image reconstruction, hardware design, circuits and systems, machine learning, biological tissue, application. In literature searching, use Boolean "or" to incorporate alternative spellings and synonyms, and use Boolean "and" to link the major terms. Alternative spellings and synonyms for major terms are also used.

2.3. Selection criteria

Inclusion criteria were based on the relevance of the article to the study, year of publication, empirical results and theoretical framework. Research and analysis of relevant electronic resources (e.g. papers, keynote addresses, etc.) for the years 2016–2022 was primarily conducted.

The initial search yielded over 22000 studies about EIT. Thereafter, the papers were screened and those that were not relevant to the title terminology were eliminated. Elimination of duplicate papers (the same paper but from different databases) was also carried out. Thereafter, elimination was based on the content of the articles. The selected articles provided information on EIT measurement principles, hardware design, applications and recent advances. In total, 120 articles were reviewed following the selection process. The articles were peer-reviewed and published in reputable journals and conference proceedings and were written in English.

3. EIT methodologies

3.1. Bio-tissue dielectric properties

The dielectric properties of biological tissues are related to their microstructure and vary over a wide frequency range from Hz to hundreds of MHz. Determined by the composition and size of the cells, the internal structure and arrangement. The cell membrane, the intracellular fluid and the extracellular fluid in the tissue change in activity corresponding to the state of the tissue. The cell membrane, the intracellular fluid and the extracellular fluid in tissue are changing in activity corresponding to the state of the tissue. An electrical field was imposed on the tissue and electrons inside the tissue excited the polarization and orientation polarization. Leading to the differences in impedance in the cytosol and the dielectric properties between cell membranes.

The impedance data of biological tissues is measured using either the two-electrode approach or the four-electrode method. Fig. 1 (b) shows a simplified equivalent model of biological tissue impedance. Where Ri, Re and Cm represent the internal and external fluid equivalent resistance and equivalent membrane capacitance of the whole biological tissue. A sine current signal ($I_b = I_m \sin\omega t$) was excited on the target, and the developed voltage signal is a sine signal of $V_m\sin(\omega t \pm \theta)$, which will be used to calculate the complex electrical impedance Z_b [44].

$$Z_b = \frac{V_b}{I_b} = \frac{V_m \sin(\omega\ t \pm \theta)}{I_m \sin\omega\ t} = \frac{|V|\angle \pm \theta}{|I|\angle 0} = \frac{|V|}{|I|}\angle(\pm\theta - 0) = |Z|\angle \pm \theta \tag{1}$$

where $|Z|$ and θ are the amplitude and phase angle, as shown in Fig. 1(c) ω is the angular frequency, I_m、$|I|$ are the maximum (peak) value and the magnitude (amplitude) of the sine current signal (I_b). V_m、$|V|$ are the maximum (peak) value and the magnitude (amplitude) of the measured voltage V_b.

For EIT, the boundary voltage was measured using the four-electrode method and a spatial physical model of the electrode positions was established. Maxwell's system of equations was used to construct a forward problem model for the injection current I_b, the

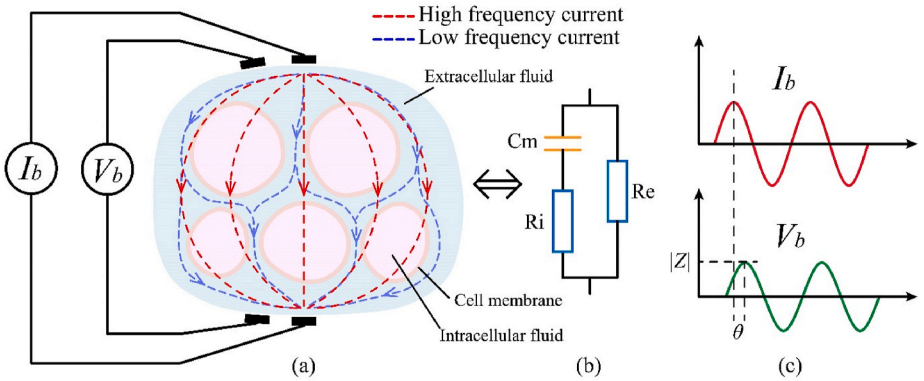

Fig. 1. Biological tissue equivalence model.

measured voltage V_b and the conductivity distribution σ^*. The inverse problem minimises the difference between the estimated voltage of the forward problem and the actual measured boundary voltage to solve for the true conductivity distribution. The total complex conductivity σ^* arising due to charge conduction and polarization mechanisms is given by equation (2):

$$\begin{aligned} \sigma^* &= (\sigma_a - i\omega\varepsilon) \\ \sigma_a &= \sigma_a{}' + i\sigma_a'' \\ \varepsilon &= \varepsilon' + i\varepsilon'' \end{aligned} \tag{2}$$

σ_a and ε denote the complex conductivity and complex permittivity, and the superscripts $'$ and $''$ correspond to real and imaginary components, respectively. ω is the angular frequency of the applied electric field. When $\omega \to 0$, the total conductivity is mainly controlled by the complex quantity σ_a consisting of electrolytic and surface conducting mechanisms. When $\omega \to \infty$, the complex dielectric constant has a significant effect on the total conductivity [45]. As shown in Fig. 1(a), the low-frequency current will flow mainly through the extracellular fluid inside the biological tissue. In this case, the impedance characteristics are mainly influenced by the extracellular fluid and the anisotropic differences are higher. High-frequency currents can cross the cell membrane, when the total impedance of the tissue fluid and membrane is measured, with less anisotropic differences [46].

Previous reviews have described the workflow and model of the EIT hardware without a detailed discussion of the details in the hardware design [47] or only the application scenarios of biological tissues under containers (Petri dishes) [48].

3.2. Stimulation and measurement model of EIT

The EIT reconstructs the distribution of conductivity and dielectric constant according to the relative spatial position and electrical properties of the target, and a 2D or 3D image to detect or anticipate the organism's state, as shown in Fig. 2. The current is not confined to the plane of the electrode array but propagates over a 3D space within the bulk conductor. The difference between 2D and 3D EIT hardware-wise was that 3D EIT requires a larger number of channels and arranges the electrodes in three dimensions [49]. The 2D image interpolation to generate the 3D structure was used more often. Real 3D EIT means that the boundary voltage on each electrode layer pair was measured for reconstruction under a set of excitations, which multiplies the measurement points, slows down the measurement and also increases the reconstruction calculation.

EIT techniques can be divided into static, time difference (TDEIT) and frequency difference (FDEIT) according to the imaging method, with TDEIT and FDEIT being more commonly used in practice [50]. TDEIT uses different Spatio-temporal correlation behavior of the target at the same excitation frequency at different times for imaging and it is suitable for situations where the conductivity of the target varies considerably over time, typically in artificially set-up saline tank and Petri dish experiments. Unsuitable for long-term monitoring situations where the background medium evaporates or cell metabolism because of the loss of the initial background as a reference. However, FDEIT uses different frequency-dependent behavior of the target at different excitation frequencies at the same time for imaging and is generally used when the impedance of the object to be measured varied insignificantly with time [51]. FDEIT require multi-frequency EIT (MF-EIT) systems, which superimpose sine waves of multiple frequencies to generate excitation signals, and then demodulate the impedance information at different frequencies from the multi-frequency signals [52].

According to the excitation and measurement modes, the EIT technique can be subdivided into adjacent, opposite and cross, as shown in Fig. 3. The excitation and measurement modes affect voltage-sensitive regions, which makes the spatial resolution of the reconstructed image non-uniform [53]. For example, the sensitivity of adjacent excitations decreases from the boundary to the centre of the target [54]. Increasing the number of voltmeters can significantly increase the speed of measurement, and EIT can be subdivided into serial, parallel and semi-parallel. The more voltmeters there is the faster the measurement, but the higher the requirement for consistency between voltmeters.

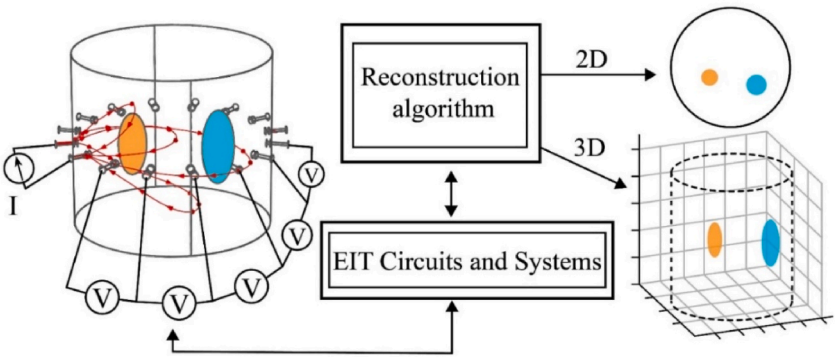

Fig. 2. EIT measurement workflow.

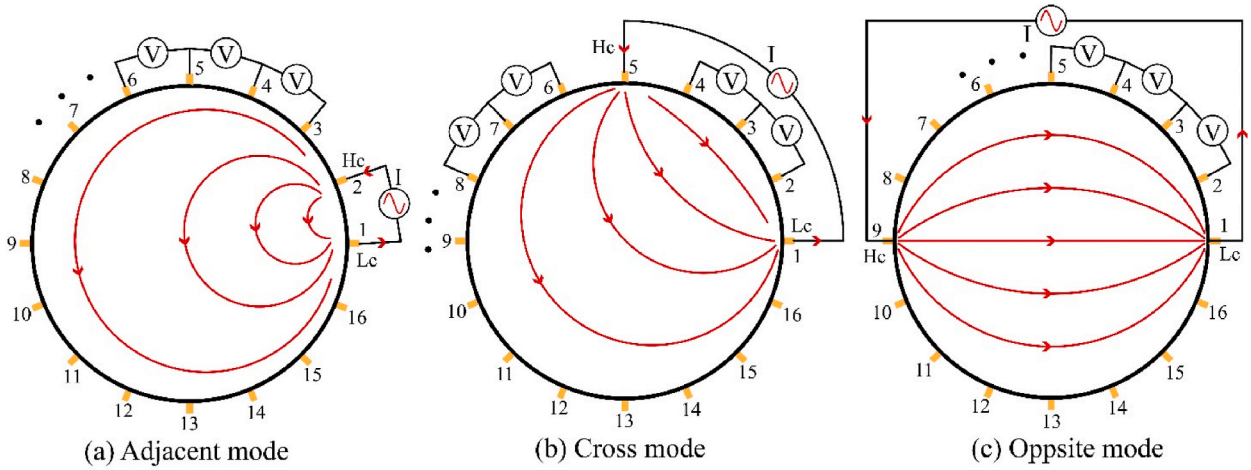

Fig. 3. Excitation and measurements modes.

3.3. EIT reconstruction

3.3.1. Forward and inverse problems

The EIT reconstruction problem is the problem of finding the internal conductivity distribution of an object when a set of injected currents and measured potentials are known. In mathematical terms, it is a non-linear inverse problem that is ill-posed. A common approach to solving such numerically ill-posed problems is to add some a priori information to the solution. The technique of replacing the original problem with a neighboring fitness problem is known as regularisation.

The forward problem solves the controlling equations of the EIT and calculates the boundary potential simulated by a known constant current in PC. The forward problem typically creates a finite element model (FEM) that matches the contour shape of the test target as a boundary condition to calculate the nodal potential in the discrete domain. Then the calculated potential data (V_c) is compared with the measured potential data (V_b) ($\Delta V = V_b\text{-}V_c$). The forward problem constructs a sensitivity matrix called the Jacobi (J), which is used by the inverse solver.

The inverse problem uses the voltage difference vector (ΔV) and the sensitivity matrix J to calculate the conductivity distribution, correcting or updating it to modify it to minimise ΔV. Each voltage difference vector has a corresponding sensitivity matrix. If the conductivity changes at the kth element, the sensitivity J_k represents the magnitude of the change in the boundary voltage. The voltage difference vector (ΔV) can be used for TDEIT or FDEIT. The inverse solver repeats the forward problem and attempts to calculate the approximate conductivity distribution. The estimated voltage change is calculated from the sensitivity matrix J and the estimated conductivity change $\Delta\,\widehat{\sigma}$.

EIDORS provides algorithmic procedures for reconstructing electrical conductivity [3,55]. Liu et al. built an open-source Python-based electrical impedance tomography library, called pyEIT [56]. Coxson et al. modified the forward solver of pyEIT to include the full electrode model (CEM) [57].

3.3.2. EIT and machine learning

With the development of EIT, machine learning methods have been introduced into the EIT field. The applications of machine learning in EIT are mainly divided into 1) solving the image reconstruction problem and 2) solving the image analysis problem after image reconstruction.

Traditional methods of image reconstruction based on regularisation to solve non-linear least squares problems have problems such as low accuracy, poor noise immunity and long computation times. There is no ideal method for data reconstruction and analysis in the reconstruction process [58]. According to the specificity of the problem to be solved, the right choice of method and model needs to be applied. For this reason, there is a new research trend to use machine learning to solve image reconstruction problems. Machine learning for EIT image reconstruction can be divided into 1) The forward and inverse problem is expanded into the network for a limited number of iterations. 2) skipping the forward and inverse problem and predicting the conductivity distribution by training the model and 3) image post-processing techniques.

However, it is necessary to verify whether machine algorithms are superior to the classical, known deterministic methods belonging to the Gauss-Newton approach. Rymarczyk et al. compared low angle regression (LARS), Elastic Net, and Multiply Neural Networks with classical Gauss-Newton and showed that artificial neural networks (ANN) achieved the best reconstruction quality [58]. Machine learning can not only improve the quality of image reconstruction but also reduce computational time. Darma et al. used the k-nearest neighbour (k-NN) algorithm to approximate the Jacobi matrix to improve the reconstruction speed. The reconstructed target conductivity components were clustered to obtain high accuracy, finally, the image edges were sharpened using Canny algorithm [59]. Chen et al. predicted the location and shape of the target by the deep neural network, then encoded the structural information as group sparse (GS) regularisation to further estimate the conductivity of each object [60].

Measurement voltage mapping to conductivity distributions is a fast method, but it requires a large dataset to train the model parameters. Hamilton et al. combined D-bar with CNN to build a mapping model and demonstrated that CNN can learn to remove blur from images effectively [61]. Chen et al. added a fully connected layer before the U-Net structure to generate an initial guess of the conductivity distribution which was sent to a denoising model for a reconstructed image [62]. Fan et al. proposed compact neural network architectures for forward and inverse problem mapping for 2D and 3D problems, respectively [63]. In contrast, unfolding the forward and inverse problems to the network with a finite number of iterations can combine the advantages of physical model-based approaches and deep neural networks [64].

Machine learning has also been used for qualitative analysis of the target's physiological state. Zhang et al. introduced a wearable wristband that uses a support vector machine (SVM) to classify sets of gestures, envisioning the integration of this technique into future smartwatches [65]. Dunne et al. used an SVM classifier to classify bladder status on a complex dataset with different bladder volumes and urinary conductivity [66]. Wu et al. used neural networks to establish links between EIT and hand prostheses [35]. Jiang et al. used a Fine Tree to classify bioimpedance data for eight gesture measurements collected by a 16-electrode EIT [36]. McDermott et al. used SVM to identify and differentiate between bleeding and clots in human data with an average accuracy of 85% [67]. Pessoa et al. applied machine learning to the diagnosis and monitoring of patients with lung disease. Several machine learning algorithms were used to classify samples, such as linear discriminant analysis (LDA); support vector machines with radial basis function kernels (SVMrbf); decision trees (DecTree); random undersampling boosted trees (RUSBoost); and random forests (RndForest). Demonstrate the potential of pairing EIT data processing and feature engineering with machine learning classification models [68].

Some scholars have also adopted machine learning methods for both image reconstruction and analysis. Husain et al. proposed a framework for artificial skin sensors. Firstly, the FEM grid is divided into n meshes, and the conductivity of each mesh was trained and predicted using low-order binary polynomials and RBF networks. Then, the reconstructed image was segmented using convolutional neural networks and migration learning. Finally, a set of object descriptors were extracted from the segmented images and the objects were classified using a KNN classifier [69].

Recently, data-driven or learning-based approaches have become the next frontier in EIT. Although these techniques could need a lot of training time and rely heavily on the quality and availability of training datasets. However, the demand for image quality and the increase in computing power has contributed to their growing popularity.

The early literature focused on the use of AI techniques to solve EIT inverse problem and clinical applications [70]. Whereas we have focused on the development of EIT hardware, a brief overview of cutting-edge AI-based EIT developments is also provided.

4. Key technique for EIT hardware

The core task of the EIT hardware is to provide a stable excitation signal and measure the amplitude and phase of the response signal accurately and quickly. The range of bioimpedance impedances is from hundreds to tens of thousands, and the SNR must be high enough to measure a broad range of impedance information. The EIT architecture typically consists of an excitation source, voltmeter, demodulator, sampling, channel network, electrodes, and power supply, as shown in Fig. 4. The EIT hardware aims at 1. high SNR; 2. fast scanning; 3. flexible channel switching schemes; 4. multi-frequency excitation and demodulation capability. EIT system performance can be quantified with common mode rejection ratio (CMRR) [71], SNR [72], reciprocity error (RE) of the channels [73], sampling rate [74], power consumption [22] and physical size.

4.1. Microcontroller

The microcontroller in the EIT system is in charge of the system's digital signal processing, channel switching, computer communication, direct generation or controlling the Direct Digital Frequency Synthesis (DDS) unit to generate sine waves as well as setting up the ADC to acquire signals and a small part of the arithmetic. The choice of microcontroller depends on the functional requirements of the EIT system and is designed using mainly FPGAs, DSPs, and single-chip microcontrollers.

The single-chip microcontroller can meet most EIT system requirements for preliminary design. The single-chip microcontroller

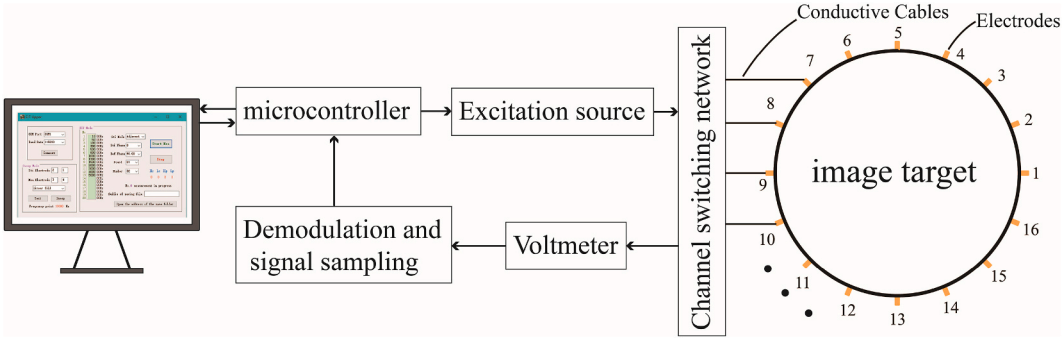

Fig. 4. Main hardware modules of EIT system.

contains the necessary digital peripherals for EIT such as serial ports, ADC modules, and general-purpose I/O ports. Dimas et al. designed a 64-channel EIT system using Arduino Due development board [75]. San-Pablo-Juárez et al. use Arduino to drive DDS, relay modules, LCD touchscreens and ADCs and solve forward problems in EIT in STM32F4Discovery [76]. Microcontrollers generally cannot generate sine signals, digital demodulation and other more complex function, limiting the system's multi-frequency capabilities.

FPGAs can perform sine wave generation and frequency superposition, multi-frequency demodulation, and digital filtering, reducing system complexity and providing excellent flexibility in excitation patterns and signal processing. McCann et al. designed the fEITER system using an FPGA to synthesise sine waves, control CMOS switches to switch channels, and implement phase-sensitive demodulation (PSD) [77]. Yang et al. generated multi-frequency superimposed excitation signals from 10 kHz to 1 MHz and demodulated the acquired multi-frequency signals inside the FPGA [72,78]. Baidillah et al. built adaptive noise cancellation (ANC) algorithms filters inside the FPGA to eliminate time-varying random noise signals [79].

Woo et al. designed the KHU Mark1, Mark2 and Mark2.5 with a master controller based on a DSP that receives commands from the PC and controls all functions of the EIT system. The system contains several impedance measurement modules (IMMs) which are independent of each other and controlled by separate FPGAs. Each IMM includes digital waveform generation, phase-sensitive demodulation, data exchange and control functions. The master controller DSP can broadcast commands to all IMMs synchronously or send commands to specific IMMs. The master-slave design allows the master to control multiple slaves synchronously for multi-channel parallel measurements [80–82]. Tran et al. sent trigger signals to the multiplexer and microcontroller based on TI's DSP processor TMS320VC5509A to synchronise ADC data acquisition and current source injection [83]. Xu et al. used the commercial Red Pitaya STEMlab to develop the EIT system for excitation signal generation, signal acquisition, AD and DA conversion, amplifier and low-pass filtering, and communication with a PC [84].

4.2. Excitation source

The design of the current source has a direct impact on the overall performance of the EIT system. Firstly, especially for human detection, the current amplitude of the current source is within the safe range. Davidson et al.'s brain function EIT system [12], McDermott et al.'s brain health monitoring EIT system [85], and Hong et al.'s early breast cancer EIT IC [21] comply with the medical device standard 60601-1. This standard limits amplitudes of the order of μA at frequencies up to 1 kHz, rising to a 10 mA limit for frequencies over 100 kHz [85]. KHU Mark 2.5 approved for medical use (ECM100US07, ECM100US09, XP Power Limited, Singapore) [82]. Yang et al. adopted the International Electrotechnical Commission (IEC) specifying a "patient auxiliary current" limit of 100 μA from 0.1 Hz to 1 kHz [86]. Yang et al. connected a resistor in series with the current output and measured the current amplitude across the resistor in real-time, allowing a current source to be turned off when the setting is exceeded [72,78].

The ideal current source has infinite impedance and a linear connection between the control voltage and the output current (transconductance), allowing for a steady constant current output. However, the current source does not remain constant in operation due to the manufacturing process, parameter precision, temperature drift of analogue circuits, and dispersed capacitance incorporated in the circuit design. In practice, the output impedance of a current driver should be high enough to provide the correct current injection, needing larger than 1 M in the frequency band [87].

Due to the manufacturing process and accuracy, the excitation frequency of EIT systems is currently in the 10 MHz range. The Howland current source (HCS) and its variations are the most commonly used, and their performance is determined by the op-amp specification and how well the resistors are matched [88]. To get a high output impedance, the op-amp should be selected for high-frequency response and open-loop gain, and minimal resistor tolerance. However, when the frequency increases, the output impedance of the HCS continues to decline. To calibrate the current source output, the KHU Mark series systems use HCS with numerous generalised impedance converters (GIC). The KHU Mark2 calibrates the current source with a digital potentiometer to have a minimum output impedance of 1 M over the whole specified bandwidth. The tuning parameters of the HCS and the GIC were discovered to interact during calibration, making parameter tuning a difficult job [82]. Shi et al. and Shishvan et al. both constructed current-detecting channels to correct output current to achieve greater output impedance [14,89]. Wu et al. and Yoo et al. used MOS tubes to build current driver ICs to obtain high-performance current sources. To obtain high-performance current sources, Jang et al. and Constantinou et al. employed MOS tubes to develop current driver IC [88,90]. Table 1 contains statistics about the current source

Table 1
Current source Comparison.

References	Output impedance	Manufacturing process	Voltage and max current range
2007 KHU Mark1 [73]	1 MΩ @500 kHz	Separated component	N/A
2010 KHU Mark2 [71,91]	greater than 1 MΩ@1 MHz	Separated component	N/A
2014 KHU Mark2.5 [92]	at least 1 MΩ in the entire frequency range	Separated component	N/A
2009 Hong et al. [93]	160 kΩ@1 MHz	0.35 μm CMOS	±2.5 V 1 mA
2014 Constantinou et al. [88]	665 kΩ@ 100 kHz 372 kΩ @ 500 kHz 64 kΩ @1 MHz	1.6 μm CMOS HV	±9 V 5 mA
2017 Wu et al. [94]	750 kΩ @500 kHz	0.18-μm CMOS	±1.65 V 1 mA
2017 Jang et al. [95]	1 MΩ @1 MHz	65 nm CMOS	1.2 V 400uA
2018 Rao et al. [26,27]	100 kΩ @1 MHz	0.18-μm CMOS	3.3 V 1 mA

design.

The common-mode voltage supplied into the measuring circuit should be kept to a minimum by the current source. Single-ended current sources discharge the excitation current by directly grounding the negative excitation electrode, resulting in large common mode voltage errors. A double-ended floating type current source, which generates a floating structure at the load side to improve noise rejection and reduce contact impedance, is the most common use. Li et al. designed a Voltage Controlled Current Source (VCCS) circuit that included a current feedback circuit as well as a differential mirror circuit. The symmetrical design increases noise rejection and lowers common-mode-caused errors [96].

4.3. Channel switching network

The channels should be numerous and flexible enough that the ideal research design could generate all feasible electrode-addressing configurations. The quality of the reconstructed images is then evaluated using a large number of simulated target placements or other sensitivity criteria [97]. There are two main types of channel design, one comprising reed relays and the other using analogue channel chips. Reed relays are internally mechanically switched and have an extremely low on-resistance Ron and distributed capacitance [CD, CS (On)]. However, the disadvantages of reed relays are obvious, as they are often big and cannot be directly driven by the controller signal. The switching time of reed relays is typically in the ms range, limiting the overall system speed. The multiplexer chip, which is compact in size, has a switching time at our level, and can be driven directly by the controller signal, is the most commonly used solution today. On the other hand, the multiplexer is constructed internally from MOS tubes, and when a channel is turned on, there is an on-resistance Ron and a switching capacitor [CD, CS (On)] at both ends of the channel. The multiplexer is linked in series with the measurement target and the current source. When the Ron resistance is high, the excitation source's output current is reduced, and the measuring range is reduced. The measurement channel is a voltage signal, and the analogue channel is connected to the electrode and voltmeter. Shi et al. use multiplexers in the boundary voltage measurement circuit to link to the outputs of these voltage followers. In this manner, the stray capacitance of the multiplexer does not reduce the measuring circuit's input impedance [14].

The MAX4545 was used to construct a channel-switching network in the KHU Mark1, Mark2, and Mark2.5 [71,80,92]. Dowrick et al. used the ADG714 to implement current injection and electrode measuring [98]. Wu et al. employed ADG1211 as the excitation path and ADG1213 as the voltage-sensing path [99]. Yang et al. designed the mfEIT system with 32 dual single-blade, single-throw switches for current injection switching and two cascaded 8×16 crosspoint switch arrays for channel selection for induction voltage measurement [72,78]. Hong et al. designed T-switches for 32-electrode lung ventilation detection [100] and 92-electrode breast cancer detection [21] EIT systems.

The parallel EIT system enables simultaneous signal capture at all electrodes without the need for a channel-switching network. The downsides are hardware complexity and symmetry, as each electrode contains a dedicated current source and voltmeter. Russo et al. used a data collection card to directly measure the voltage at the electrodes [101]. Kim et al. incorporated a current source, voltmeter, analogue channel, and communication module into an active electrode IC, allowing them to control the stimulation or measurement of each electrode independently, significantly boosting system speed [8,9].

4.4. Electrodes & conductive cables

The flexible electrode design expands the spectrum of EIT applications. EIT is dependent on the electrode making direct touch with the object being monitored, and the degree of coupling on the contact surface is often undesired and inhomogeneous. Researchers explored the quantity, material, and geometry (form and size) of electrodes.

Ag/AgCl electrodes have the low contact impedance ($p > 0.05$), high SNR (60.3 ± 4.5 dB), excellent uniformity (correlation coefficient 0.95 ± 0.03), and higher overall best performance stability (slope 0.68 ± 0.03) as commercial ECG electrodes in medical imaging EIT [13,102]. To create optimal electrical contact between the electrode and the subject's skin, conductive gels are frequently utilized [86]. Hong et al. designed 90 Ag/AgCl soft electrodes for a breast detection EIT electrode array [21]. Woo et al. developed an elastic electrode belt with a PEDOT coating [103]. Gold-plated electrodes are resistant to corrosion, and Yang et al. created a 3D image EIT sensor for cell imaging. Tissue cells are cultivated in a culture solution, and the electrodes are printed on a circuit board and gold-plated to avoid corrosion from the solution and electrochemical reactions [30,104].

Larger electrodes reduce the contact area but increase the distance between electrodes and influence detection depth in some excitation modes [105]. An increasing number of electrodes increases the spatial resolution, but the acquisition time increases, limiting the system's temporal resolution. However, as the number of electrodes rises, the measured voltage difference decreases, resulting in a worse SNR [106]. Fabrizi et al. showed that 16 electrodes were more effective than 32 electrodes and that a higher number of electrodes did not always increase image quality [97]. Furthermore, managing the circuit wiring and wire shielding between the electrodes and the EIT system not only limits the EIT's practicality and mobility, but the dense wiring raises the risk of stray capacitance and crosstalk.

The electrode arrangement method and the excitation measurement mode affect the imaging sensitivity region. Kwon et al. demonstrated experimentally that by altering the density of the electrode layout, the internal local area resolution could be enhanced [107]. The electrode position is not perfectly accurate, especially in human testing, as the electrode position changes with the patient's physiological activity. The accuracy of the electrode position is critical for EIT forward and inverse problem-solving. Wu et al. integrated accelerometer sensors on sensing electrodes to detect the patient's chest shape and electrode position in real-time to help calibrate the orthogonal problem model [108]. However, because of the additional hardware required, this solution is often more

expensive and complex.

Contact impedance influences current distribution beneath the electrodes, and too high contact impedance can saturate the signal and preclude the acquisition of a reliable boundary voltage signal. An imbalance in contact impedance between the two measurement electrodes might cause a common mode voltage to generate a differential mode signal at the preamplifier's input, resulting in image artefacts [86]. The contact impedance between the skin and the electrode cannot be neglected in medical applications. Hong et al. created the P-FCB electrode to fit the skin for this purpose, which normally has an electrode-skin contact impedance of 300 Ω at 10 kHz [100]. Ma et al. employed SPDT to switch between the contact impedance measurement mode and EIT operational mode during the measurement to measure the contact impedance between the functional and reference electrodes in real time [16]. Hong et al. designed the pulmonary ventilation EIT IC to measure contact impedance every 1 min, categorising electrode contact impedance into four categories (Good, Average, Bad, and No contact) and readjusting the electrode strip to fit the chest if more than three non-contact electrodes were used [100]. Stereotactic electrodes are more stable than flat electrodes and have a lower contact impedance. The contact impedance decreases with electrode depth (or with pressure applied to the skin). The contact pressure between each electrode and the skin can be flexibly modified to adjust contact impedance thanks to a miniature electrode unit created by Avery et al. and controlled by a servo [109]. Sakai et al. designed the elastic suit with dual-planar EIT electrode arrangement to suit the skin for proper daily monitoring of gastric function [110].

Long cables are frequently used by EIT data acquisition systems to connect to the electrodes, and the electrodes can be configured using a channel-switching network. To minimise the variation in impedance caused by wire length differences, we recommend that all wires of the electrode and circuit be of the same length. If the object to be monitored is immersed in liquid, we recommend coating the electrode with platinum black to enhance the contact surface without increasing the volume, reducing polarization effects and contact impedance. The gold plating on the electrode surface, which has great biocompatibility and stability, is best suited for long-term monitoring situations. A voltage-driven coaxial wire shield, as shown in Fig. 5, is advised to reduce noise, stray capacitance, and leakage currents.

Gaggero et al. presented the concept of active electrodes in 2012 [111]. Active electrodes reduce parasitic capacitances of several hundred pF caused by cable and channel switching networks to a few pF [99]. Wu et al. incorporated a current source and voltmeter into the active electrode [112], exposed the electronic device to parasitic capacitance effects by bringing it into direct contact with the electrode, and compared the parasitic capacitance effects of the active and passive electrodes [113]. Jang et al. developed a portable, low-power, high-precision active electrode with a current source, voltmeter, and phase correction circuit [95].

4.5. Voltmeter

The boundary voltage signal at the measurement electrodes is carried to the voltmeter after the current has flowed through the target to be measured. EIT commonly employs four-electrode measurement, which has the advantage of requiring less dynamic range from the voltmeter because the voltage between a pair of electrodes is less than the voltage between each electrode and ground potential.

The polarization of the electrodes creates a chemical battery, which generates a DC voltage across the electrodes. Because the polarity and amplitude of the DC component at each electrode are uncertain, additional circuitry is required to isolate the DC in the

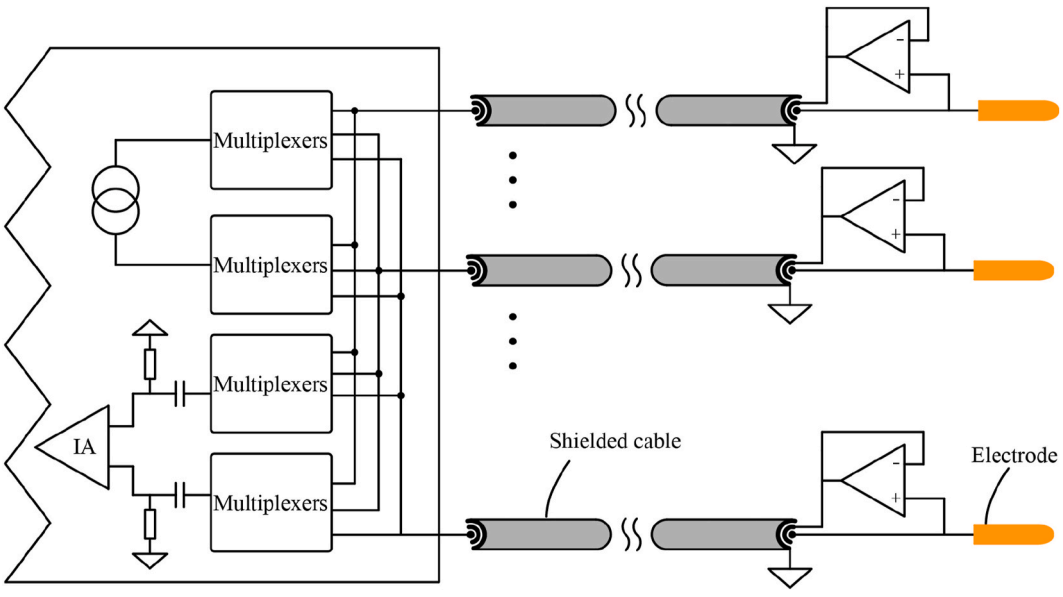

Fig. 5. Voltage-driven triaxial cables using a voltage follower.

voltmeter. The signal must be filtered out of the DC component before amplification to avoid saturation of the input signal due to DC bias, and maximise dynamic range, and SNR. As shown in Fig. 6(a), the DC component is filtered before entering the amplifier, while Fig. 6(b) amplifies the signal directly, resulting in distortion as the amplified signal is outside the effective range of the device. Isolated DC circuits typically employ first-order RC high-pass filters, the cut-off frequencies and build-up times of which can be easily calculated using simulation. The longer the filter build-up time, the lower the excitation frequency. Lee et al. created a filter with a current drain circuit to quickly drain current from the filter capacitor. When the electrodes are switched, the drain circuit is turned on and connected to the ground for 0.5 excitation cycles to reduce the time required for stabilisation [114].

Voltmeters require a high input impedance to prevent current from flowing through the amplifier, causing a loop and an undesirable voltage drop with the contact impedance [102]. The preamplifier's input impedance should be much bigger than the contact impedance (at least 1000 times). Therefore, high common-mode rejection ratio amplifiers with very high input impedance and common-mode rejection ratio (CMRR) as well as low input capacitance are usually used in preamplifiers. Dimas et al. employed the instrumentation amplifier (IA) AD8421 to amplify the signal after isolating the DC [75]. Shi et al. employed a low-noise IA, the INA163, as a preamplifier and followed it with a broadband programmable gain amplifier (PGA), the THS7001, for gain control [14].

The transient reaction in the measurement circuit while switching the excitation electrode pair has a substantial impact on the voltmeter's acquisition accuracy. The typical way for obtaining precise measurement findings is to wait for more cycles for the response to dissipate, although this strategy increases the sampling time. Li et al. [96] and Lee et al. [74] control the switching of the excitation electrode pair at the AC signal crossing point to assure sampling accuracy and reduce waiting time.

Simultaneous measurements utilising numerous voltmeters are referred to as parallel or semi-parallel systems, and they can be useful in enhancing measurement speed and system time resolution [101]. The foundation of parallel EIT systems is high symmetry between parallel channels. Yang et al. designed a two-channel semi-parallel EIT in which two channels can acquire data at the same time [72]. Hong et al. designed a 6-channel semi-parallel EIT system [100]. Mi et al. attempted to develop a 16-channel parallel EIT system using a PGA and a 12-bit ADC for each channel [115]. The above-mentioned active electrode EIT is likewise a fully parallel technique.

4.6. *Demodulation and signal sampling*

The impedance of biological tissue comprises both the resistive and capacitive components, and the signal must be demodulated using phase-sensitive demodulation to get the real and imaginary components. In-phase and quadrature-phase (I-Q) demodulation is the most prevalent type of demodulation (also known as coherent demodulation or synchronous detection). The measured signal is multiplied by the 0° and 90° reference signals, and the remaining DC component after low-pass filtering is the demodulated signal. This

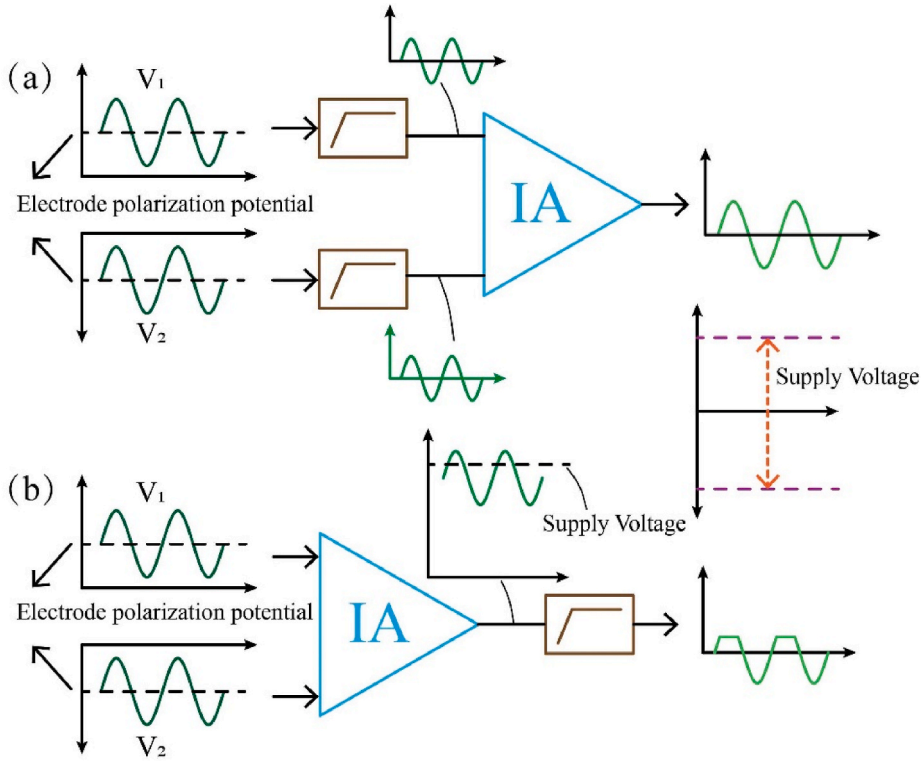

Fig. 6. Isolated DC and amplifier circuit.

method can be extended to multi-frequency demodulation. As excitation signals, the MF-EIT superimposes sinusoidal signals of various frequencies, and the boundary voltage carries impedance information at various frequencies [116]. I-Q demodulation can demodulate multiple impedance information based on the frequency of the reference signal, as illustrated in Fig. 7.

Demodulation is classified into two types: analogue device demodulation and digital demodulation. The sample rate required by the ADC depends on the demodulation process. The analogue device demodulation pre-stage circuit converts the AC signal to a DC voltage without requiring a high sampling rate from the ADC. It should be noted that, as shown in equation (1), the phase angle might be negative, resulting in the generation of negative voltages during the analogue demodulation process. Therefore, a bipolar ADC or an operational circuit must be used to adjust the voltage amplitude to a tolerable range. An analogue multiplier and a low-pass filter are typically used in analogue demodulation. Due to the restrictions of capacitor charge and discharge times, increasing the speed of demodulation is challenging. Engineers can acquire parameters such as filter build-up time, cut-off frequency, and ripple using simulation tools such as Spice.

Digital demodulation necessitates the collection of the AC signal to the controller first, and digital demodulation techniques are more flexible. The Shannon sampling theorem states that the sampling frequency should be at least twice the highest in the analogue signal spectrum to retrieve the analogue signal without distortion. It is recommended that the ADC sampling rate surpasses the signal frequency by a factor of 10 or more for practical EIT applications [121]. The minimum sample rate of the ADC is determined by the excitation frequency when utilising the digital demodulation method. Sampling is often done using a separate ADC chip, as shown in Table 2. The ADC must modify the sampling frequency in real-time by the excitation frequency to sample the same number of points at different excitation frequencies [78,90]. Ma et al. developed the SJTU MK-1 to generate the ADC sampling clock based on the excitation frequency and sample count [119].

To get a greater SNR, the circuit noise can be reduced by raising the ADC sampling frequency and the number of sine periods sampled per measurement window. However, this also increases the total time required to measure the frame. The trade-off between signal noise and frame rate is always there [122]. The preamp output voltage should be around 90% of the ADC input range to make good use of the ADC sampling range [73].

4.7. EIT circuit calibration

EIT hardware circuits are not only sensitive to the impedance of the target but the distributed capacitance and contact impedance in the circuit board is also taken into account. Distributed capacitance generates frequency-dependent current leakage in the circuit, resulting in an applied current that is not equal to the current provided by the current source. The parasitic capacitance and system error sources are typically stable over short periods and can be reduced by TDEIT. Contact impedance reduces with frequency but can still be several hundred ohms at 100 kHz in brain detection, which might severely alter bioimpedance studies [102]. As indicated in Fig. 8, where R_o and C_o are the current source's output impedances, and ΔI represents the leakage current across the output impedance. The channel on-resistance is R_{ON}, on switch capacitance [C_D, C_S (On)]. The cable's on-resistance is R_{CB}, the distributed capacitance is C_{CB}, and *i* represents the leakage current caused by the distributed capacitance on the multiplexer and the wire. The contact impedance is Z_{CS}, and the instrumentation amplifier's input impedance is Z_{CM}.

The output impedance of the current source, as well as the distributed capacitance present in the channel switching network and cables, have the greatest impact on the accuracy of the system measurement in EIT systems. Many scholars have proposed correction or compensation schemes to address these two issues. Oh et al. subdivided the excitation frequency range and assigned a generalised impedance converters (GIC) circuit to each subrange to operate as an inductor at the required frequency interval [80]. Shi et al. detect

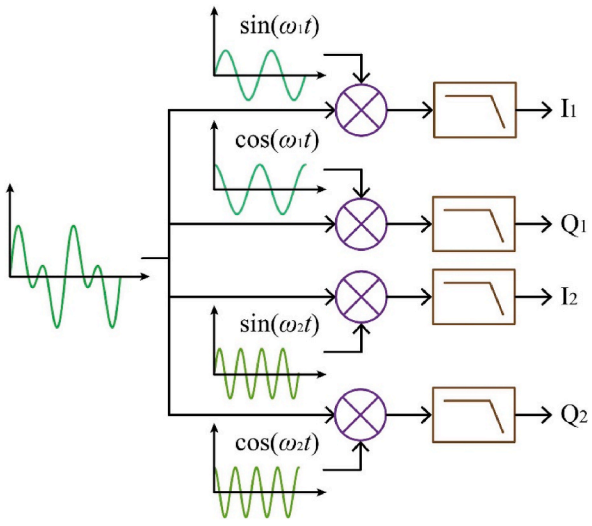

Fig. 7. Multi-frequency demodulation.

Table 2
Demodulation and sampling methods.

References	Analogue Demodulation & DC Sampling		References	AC Sampling & Digital Demodulation	
	Demodulation method	ADC		ADC	Demodulation method
2014 Lee et al. [23]	Analogue Multiplier low Pass filter (I-Q)	625 kHz ADC	2018 Wu et al. [117]	AD7357 4 MHz ADC	MAC units (I-Q)
2015 Hong et al. [21]	Peak-to-peak detector (PPD)	14-bit ADC	2018 Dong and You et al. [118]	16-bit AD7671	I-Q
2015 Hong et al. [100]	Passive mixers Low-pass filters I-Q	10-bit 200 kHz ADC	2019 Shi et al. [96]	AD79862 MHz	I-Q
			2007 KHU Mark1 [80] 2014 KHU Mark2 [91] 2014 KHU Mark2.5 [92]	12-bit 10 MHz AD9235	I-Q
			2017 Yang et al. [78]	16-bit 10 MHz	I-Q
			2018 SJTU MK-1 [119]	12-bit 32 MHz	
			2018 Darnajou [120]	NI-9223 AI modules 16-bit 1 MHz	FFT

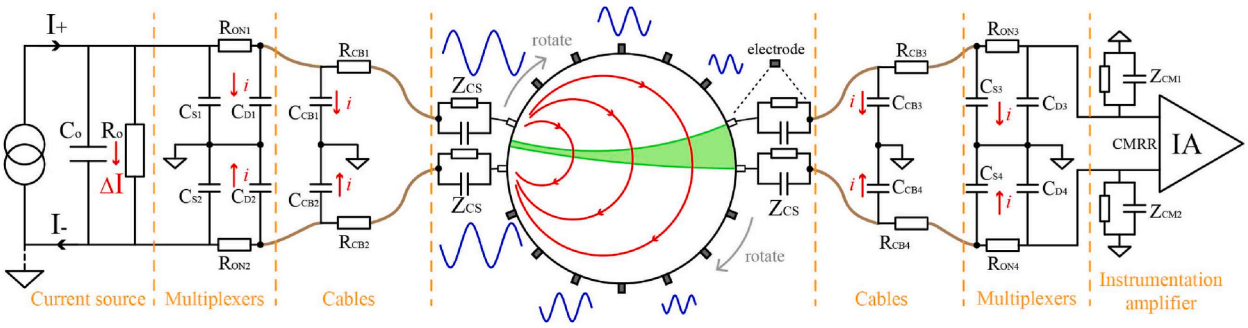

Fig. 8. Error source of EIT system.

the current magnitude using a current-to-voltage circuit and modify the output of the current source to guarantee that the excitation current is injected into the target region at the desired level [14]. Jang et al. added a current source calibration mode during which the current path to the electrodes is closed and each node drives current to a reference resistor in the calibration cell in turn. The calibration code is fed back to each active electrode IC to equalise the amplitude of each injected current. Instead of adjusting the current source directly, they used a feedback circuit made up of a phase discriminator to create a control signal that adjusted the reference signal during demodulation to produce the same hysteresis as the signal on the test resistor, thereby achieving phase correction [90, 95].

For the distributed capacitance in the channels and cables, Hong et al. connect 100 Ω resistors to the channels in turn. To calibrate each channel during EIT operation, the controller samples the voltage signal of each channel and calculates the channel gain mismatch information [21]. Li et al. corrected the results by measuring the conductivity and dielectric constant at each frequency and for each channel using a standard resistive network [96]. Wu et al. discovered that distributed capacitance induced different errors at different frequencies in FDEIT and that this impact could not be eliminated by simple subtraction. They proposed that before starting with the reconstruction, they subtract the boundary voltage under the pure substrate to remove the impacts of leakage current and contact impedance [123].

Because the current is mostly focused near its injector electrode, the resulting potential decreases as the measuring electrode is moved further from the excitation electrode, as seen in Fig. 8. The voltmeter has the same noise power, and the signal SNR at the far electrode decreases. The EIT algorithm is an ill-posed problem, and inaccuracies in a single measurement can have a large impact on the overall image [74]. To ensure a high SNR, it is desirable for the voltmeter to automatically regulate the gain by the electrode location. This makes it possible to use the entire dynamic range of the voltmeter by amplifying all measured voltage signals into the useable range of the post-stage circuit. Teng et al. presented a programmable gain instrumentation amplifier for high-speed electrical impedance tomography to overcome this issue [124].

In the process of developing a system, compensation and calibration are crucial steps, and it is more feasible to calibrate using consistent media or standardised electronic components. Finally, The measured voltage in a homogenous medium is used to evaluate the hardware voltage. Commonly used evaluation parameters are the system SNR [72], the root means the square value of relative variation to assess the repeatability of the data acquisition system [115], and the consistency of the channels calculated using reciprocity error [82]. Evaluation of the repeatability of an EIT system built by digital & analogue circuits [42] with saline tank experiment. The tank boundary has 16 electrodes, the hardware system is shown in Fig. 9(a) and the measured signals are shown in Fig. 9(b).

We employed the root-mean-square of relative changes (RMSrc) from the literature [115]. Where the radius of the saline tank was 10 cm, the excitation current was set at 1 mA and the conductivity of the brine was 0.1 S/m. The test was conducted three times on a single-layer circuit board, and the RMSrc for Test2 and Test3, using test 1 as a reference, were 4.52% and 4.38%, respectively.

5. Discussion

There is no unified specification for EIT hardware circuit design, and researchers have followed the idea of modular design, which consists basically of a controller, excitation source, channel network, electrodes, voltmeter and other parts. The SNR of EIT hardware systems currently varies from 40 to 85 dB, and in the future, increasing this SNR will continue to be a research priority. We simulated the reconstruction results for various SNR, with the background conductivity set to 0.1 S/m and the target conductivity set to 0.2 S/m, and the results are displayed in Table 3.

The most popular excitation source design is the Howland current source in current source design. As researchers demand more system accuracy and stability, Howland current sources are no longer suitable for a wide range of applications. A close match between the source and sink currents in the double-ended current source can reduce the common mode signal and contact impedance in the test [94], offering the best sensitivity for the voltage amplifier to detect tiny impedance changes [117]. To reduce the number of operational steps, the current source should feature an automatic calibration function.

Despite the numerous publications on EIT, this technique is not widely practised. This is due to the uncertainty of the electrodes' contact impedance. On the one hand, the contact impedance and the leakage current combine to generate a voltage, causing the measurement result to be affected by both the internal tissue impedance and the contact impedance. An imbalance in the contact impedance between the two measuring electrodes, on the other hand, may cause a common mode voltage to generate a differential mode voltage at the preamplifier's input, resulting in a common mode voltage in the measurement result.

There hasn't been any research into employing contact impedance measurements to improve image quality or assess the magnitude of introduced artefacts, even though methods for measuring contact impedance have been developed [16]. It is advised to use innovative materials to fabricate electrodes that are tightly coupled to the target to lower the contact impedance and make the contact impedance between the electrodes similar. We suggest including the method of detecting contact impedance in the hardware system as an input variable to the reconstruction algorithm to produce the full electrode model.

A circuit's dispersed capacitance, which is introduced by elements including channel switching networks, board materials, manufacturing thickness, electronic component tolerances, and less-than-ideal frequency characteristics, is an unknown variable. With voltage-driven coaxial cables, it is usual to reduce leakage current and stray capacitance. The idea of "active electrodes," first out in recent years [111], eliminates the need for coaxial wires by integrating the current source and voltmeter on the electrodes.

Additional system calibration is necessary to completely remove faults from the circuit. Inside the system, a resistor model is installed to calibrate the voltmeter for all channels or in parallel [82]. Further, A resistor network model is intended to hold the system's calibration parameters in distinct frequency bands [96]. As a result, as shown in Fig. 10, we have broken the EIT system setup process into four parts.

Fig. 11(a) shows the extraction of a measurement period from the voltage waveform displayed in Fig. 9(b). Fig. 11(b) shows the relationship between the amplitude of the sine wave signal before demodulation and the electrode position in the actual measurement. According to our measurements, the amplitude difference between V_1 at the top and V_7 at the bottom of the U-shaped diagram is 5–10 times. V_7's SNR is lowered by a maximum of 20 dB when compared to V_1 at the same noise level. Therefore, the measurement points at the bottom of the U-shaped diagram include a significant quantity of random noise, reducing the number of valid measurement points significantly. However, the voltage peak is restricted by the supply voltage V_{supply}, making high signal-to-noise data impossible to

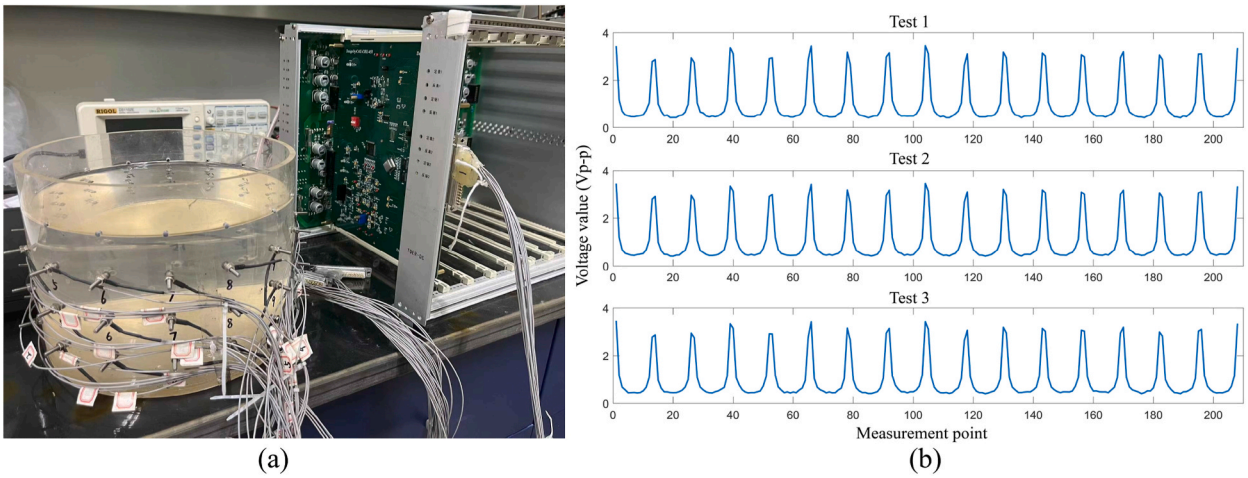

Fig. 9. Channel repeatability test of a single-layer circuit board using 16-electrode.

Table 3
Reconstruction at different SNR.

Noise level (dB)	30	45	60	75	90	No noise
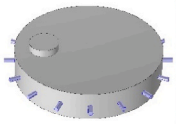						

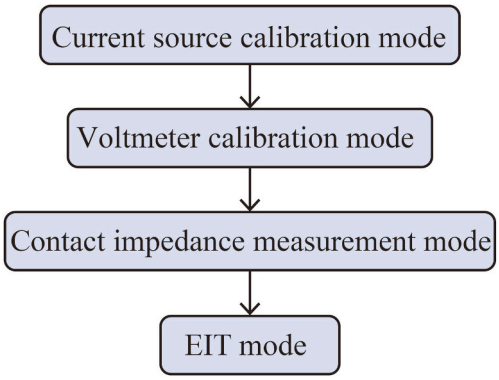

Fig. 10. EIT system setup process.

achieve if uniform amplification is applied at all measurement points. Few research teams have noticed this issue, and we advocate constructing amplifiers with adjustable amplification. The voltage is amplified to an approximate range at all measurement places, the amplified voltage and amplification information is recorded, and the true voltage at the measurement point is back-calculated in the lower or upper computer. Finally, the computation in equation (3) yields a voltage with a high SNR. Where V_a denotes the amplified voltage, k denotes the amplification factor, and V_m denotes the measured voltage.

$$V_a = k \cdot V_m \tag{3}$$

To address miniaturisation and low power consumption criteria, semiconductor manufacturers have produced specific chips for electrical impedance measurements, which package modules such as DDS units, excitation circuits, voltmeters, or ammeters on a single chip. Specialized chips, for example, MAX30009, ADuCM350, AD5933/5934, AFE4300, and AFE4500, do not often include an internal channel network, and customers must create their own to meet their specific requirements. Jiangtao Lu et al. built an 8-electrode wearable EIT sensor for hand gesture identification using the AD5933 [125]. However, the limited measuring range and low level of customising of dedicated chips limit the application scenarios. Some teams design their integrated circuit chips, with the majority of the circuitry integrated on active electrodes. The Active Electrode IC designed by Wu et al. [99] and the EIT IC designed by Lee et al. [22] are two examples. The design threshold and investment requirements for creating integrated circuits on your own are significant, and just a few teams have produced designs thus far. Google debuted their semiconductor open-source design website in June 2022, with a fully open-source process design kit (PDK) and related tools based on the 130 nm process. This gives researchers another option for designing their cross-conducting current sources or building whole EIT hardware systems.

Another major cause of artefacts in reconstructed images is the forward problem model's inability to accurately model the target domain boundaries. In recent years, researchers have attempted to gather patient body contours by integrating sensors to reconstruct high-quality images of lung breathing [108]. The image reconstruction inverse issue with EIT is nonlinear and substantially ill-posed, with slight changes in boundaries (for example, electrical noise on the electrodes) causing massive, unanticipated changes in the reconstructed image. This means that even at low noise levels, considerable artefacts might appear in the image [121]. The researchers employed a machine learning-based post-learning method to eliminate image artefacts, but how to keep relevant information in this manner has yet to be researched.

Currently, EIT approaches are generally employed to tackle qualitative problems such as determining the presence of a tumour, or stroke. As research advances, new requirements for quantitative analysis emerge. The calibration of the reconstructed conductivity at a constant frequency, current, and gain is required for the quantitative study of the conductivity distribution in the domain to be measured. The application and research of EIT is mainly focused on 2D-EIT or interpolated 3D-EIT. Real-3DEIT requires more measurement points from the viewpoint of the hardware system, and from the viewpoint of the software, real-3DEIT requires the division of more grids, resulting in a significant amount of computation for reconstruction. Real-3DEIT is the future of EIT technology and can offer a more comprehensible and intuitive view of the condition of biological tissue. Real-3DEIT's key drawback is its time expense,

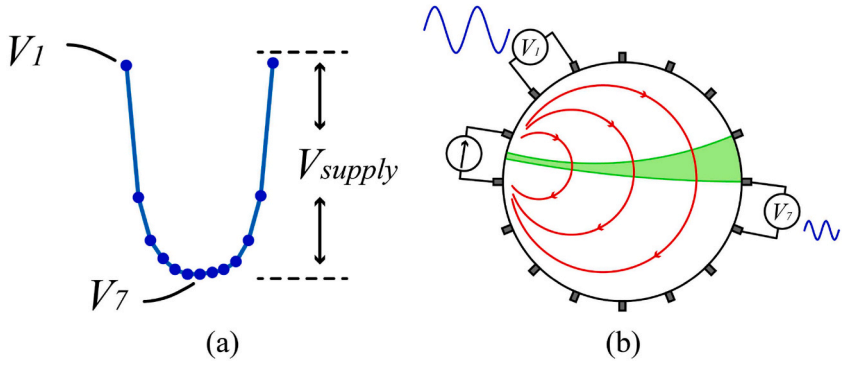

Fig. 11. SNR analysis of the measured voltage.

hence future advancements in EIT technology must focus on quick measurement and quick reconstruction of the image target. The primary goal of combining machine learning and EIT is to increase the quality of reconstructed images. The application of machine learning to improve the clarity of the demarcation boundaries between distinct biological tissues in reconstructed pictures and to aid in characterization and quantification is the general direction of future EIT development.

6. Conclusion

This paper covers the modular design architecture of EIT hardware and improvement approaches to increase the signal-to-noise ratio of the system in bioimpedance research, discusses the working principle, advantages and limits of EIT, and briefly summarises the application of machine learning in EIT. We wish to help researchers who are developing hardware solutions for EIT with a high signal-to-noise ratio and quick scanning. At present, EIT picture quality (particularly resolution) is not comparable to that of X-CT and MRI. However, the temporal and spatial conductivity provided in EIT data is extremely helpful in bioimpedance research. How to use measurement data to develop an effective link with the target's physicochemical attributes is a new topic in EIT applications. The translation of EIT technology into productivity tools still requires further development and is a challenging and open research area.

Declarations

Author contribution statement

All authors listed have significantly contributed to the development and the writing of this article.

Funding statement

This work was supported by the National Science Foundation of China, China under Grant 32171891.

Data availability statement

No data was used for the research described in the article.

Declaration of interest's statement

The authors declare no competing interests.

Additional information

No additional information is available for this paper.

References

[1] Z. Zheng, Z. Wu, R. Zhao, Y. Ni, X. Jing, S. Gao, A review of EMG-, FMG-, and EIT-based biosensors and relevant human-machine interactivities and biomedical applications, Biosensors (Basel) 12 (7) (2022).
[2] P.F. Zhao, et al., Moisture–conductivity calibration for electrical imaging of horticultural substrate, Agriculture 11 (9) (2021).
[3] A. Adler, et al., GREIT: a unified approach to 2D linear EIT reconstruction of lung images, Physiol. Meas. 30 (6) (2009) S35.
[4] J. Kuen, E.J. Woo, J.K. Seo, Multi-frequency time-difference complex conductivity imaging of canine and human lungs using the KHU Mark1 EIT system, Physiol. Meas. 30 (6) (2009) S149–S164.
[5] A. Farooq, J.N. Tehrani, A.L. McEwan, E.J. Woo, T.I. Oh, Improvements and artifact analysis in conductivity images using multiple internal electrodes, Physiol. Meas. 35 (6) (2014) 1125–1135.

[6] G.Y. Jang, et al., Imaging of regional air distributions in porcine lungs using high-performance electrical impedance tomography system, in: Presented at the 2017 39th Annual International Conference of the IEEE Engineering in Medicine and Biology Society (EMBC), 2017.
[7] M. Darnajou, et al., High speed EIT with multifrequency excitation using FPGA and response analysis using FDM, IEEE Sensor. J. 20 (15) (2020) 8698–8710.
[8] M. Kim, et al., A 1.4-mΩ -sensitivity 94-dB dynamic-range electrical impedance tomography SoC and 48-channel hub-SoC for 3-D lung ventilation monitoring system, IEEE J. Solid State Circ. 52 (11) (2017) 2829–2842.
[9] M. Kim, J. Bae, H.J. Yoo, Wearable 3D lung ventilation monitoring system with multi frequency electrical impedance tomography, in: 2017 IEEE Biomedical Circuits and Systems Conference (BioCAS), IEEE, 2017, pp. 1–4.
[10] H.F.J. Tregidgo, M.G. Crabb, A.L. Hazel, W.R.B. Lionheart, On the feasibility of automated mechanical ventilation control through EIT, IEEE Trans. Biomed. Eng. 65 (11) (2018) 2459–2470.
[11] S.Y. Qu, M. Dai, S. Wu, Z.R. Lv, X.Y. Ti, F. Fu, System introduction and evaluation of the first Chinese chest EIT device for ICU applications, Sci. Rep. 11 (1) (2021), 19273.
[12] J.L. Davidson, P. Wright, S.T. Ahsan, R.L. Robinson, C.J.D. Pomfrett, H. McCann, fEITER – a new EIT instrument for functional brain imaging, J. Phys. Conf. 224 (2010).
[13] L. Yang, et al., Optimal combination of electrodes and conductive gels for brain electrical impedance tomography, Biomed. Eng. Online 17 (1) (2018) 186.
[14] X. Shi, F. You, C. Xu, Z. Ji, X. Huo, Design and implementation of a high-precision electrical impedance tomography data acquisition system for brain imaging, in: Biomedical Circuits & Systems Conference, 2017.
[15] G. Zhang, et al., An on-line processing strategy for head movement interferences removal of dynamic brain electrical impedance tomography based on wavelet decomposition, Biomed. Eng. Online 18 (1) (2019) 55.
[16] H. Ma, et al., Real-time monitoring of contact impedance from multiple electrode–scalp interfaces during cerebral electrical impedance tomography, IEEE Access 7 (2019) 95186–95196.
[17] E.J. Woo, J.K. Seo, Magnetic resonance electrical impedance tomography (MREIT) for high-resolution conductivity imaging, Physiol. Meas. 29 (10) (2008) R1–R26.
[18] Z.J. Meng, et al., Numerical simulations of MREIT conductivity imaging for brain tumor detection, Comput. Math. Methods Med. 2013 (2013), 704829.
[19] T.I. Oh, et al., Sub-millimeter resolution electrical conductivity images of brain tissues using magnetic resonance-based electrical impedance tomography, Appl. Phys. Lett. 107 (2) (2015).
[20] O.I. Kwon, et al., Current density imaging during transcranial direct current stimulation using DT-MRI and MREIT: algorithm development and numerical simulations, IEEE Trans. Biomed. Eng. 63 (1) (2016) 168–175.
[21] S. Hong, et al., A 4.9 mΩ-sensitivity mobile electrical impedance tomography IC for early breast-cancer detection system, IEEE J. Solid State Circ. 50 (1) (2015) 245–257.
[22] J. Lee, et al., A 9.6 mW/Ch 10 MHz wide-bandwidth electrical impedance Tomography ic with accurate phase compensation for breast cancer detection, in: 2020 IEEE Custom Integrated Circuits Conference (CICC), 2020.
[23] Y. Lee, U. Ha, K. Song, H.-j. Yoo, 3.8 mW Electrocardiogram (ECG) filtered electrical impedance tomography IC using I/Q homodyne architecture for breast cancer diagnosis, in: 2014 IEEE International Symposium on Circuits and Systems (ISCAS), IEEE, 2014, pp. 2389–2392.
[24] Z. Cheng, D. Dall'Alba, P. Fiorini, T.R. Savarimuthu, Robot assisted electrical impedance tomography system for minimally invasive surgery, in: Presented at the 2021 20th International Conference on Advanced Robotics (ICAR), 2021.
[25] Z. Cheng, D. Dall'Alba, P. Fiorini, T.R. Savarimuthu, Robot-assisted electrical impedance scanning system for 2D electrical impedance tomography tissue inspection, in: Annu Int Conf IEEE Eng Med Biol Soc, vol. 2021, 2021, pp. 3729–3733.
[26] A. Rao, et al., An analog front end ASIC for cardiac electrical impedance tomography, IEEE Trans. Biomed. Circuits Syst. 12 (4) (2018) 729–738.
[27] A. Rao, E.K. Murphy, R.J. Halter, K.M. Odame, A 1 MHz miniaturized electrical impedance tomography system for prostate imaging, IEEE Trans. Biomed. Circuits Syst. 14 (4) (Aug 2020) 787–799.
[28] H. Wu, Y. Yang, J. Escudero, J. Jia, Feasibility study of frequency-difference electrical impedance tomography on industrial applications, in: 8th World Congress on Industrial Process Tomography (WCIPT), 2016.
[29] Y. Yang, H. Wu, J. Jia, P.-O. Bagnaninchi, Scaffold-based 3-D cell culture imaging using a miniature electrical impedance tomography sensor, IEEE Sensor. J. 19 (20) (2019) 9071–9080.
[30] X. Yin, H. Wu, J. Jia, Y. Yang, A micro EIT sensor for real-time and non-destructive 3-D cultivated cell imaging, IEEE Sensor. J. 18 (13) (2018) 5402–5412.
[31] Z. Chen, Y. Yang, Structure-aware dual-branch network for electrical impedance tomography in cell culture imaging, IEEE Trans. Instrum. Meas. 70 (2021) 1–9.
[32] Z. Liu, P. Bagnaninchi, Y. Yang, Impedance-optical dual-modal cell culture imaging with learning-based information fusion, IEEE Trans. Med. Imag. 41 (4) (2021) 983–996.
[33] Z. Liu, Y. Yang, Image reconstruction of electrical impedance tomography based on optical image-guided group sparsity, IEEE Sensor. J. 21 (19) (2021) 21893–21902.
[34] Y. Wu, D. Jiang, R. Bayford, A. Demosthenous, Live demonstration: a wearable EIT system for hand prosthesis motion controls, in: 2018 IEEE International Symposium on Circuits and Systems (ISCAS), 2018.
[35] Y. Wu, D. Jiang, X. Liu, R. Bayford, A. Demosthenous, A human-machine interface using electrical impedance tomography for hand prosthesis control, IEEE Trans. Biomed. Circuits Syst. 12 (6) (2018) 1322–1333.
[36] D. Jiang, Y. Wu, A. Demosthenous, Hand gesture recognition using three-dimensional electrical impedance tomography, IEEE Trans. Circuits Syst.II: Express Briefs 67 (9) (2020) 1554–1558.
[37] S. Russo, S.N. Meziani, T. Gulrez, N. Carbonaro, A. Tognetti, Towards the development of an EIT-based stretchable sensor for multi-touch industrial human-computer interaction systems, in: International Conference on Cross-Cultural Design, 2016.
[38] J. Zhu, et al., EIT-Kit: an electrical impedance tomography toolkit for health and motion sensing, in: Presented at the the 34th Annual ACM Symposium on User Interface Software and Technology, 2021.
[39] J.G. Gnecchi, A.G.-T. Chávez, G.C. Campos, V.O. Peregrino, E.M. Pineda, Soil water infiltration measurements using electrical impedance tomography, Chem. Eng. J. 191 (2012) (2012) 13–21.
[40] D.D.J. Corona-Lopez, S. Sommer, S.A. Rolfe, F. Podd, B.D. Grieve, Electrical impedance tomography as a tool for phenotyping plant roots, Plant Methods 15 (2019) 49.
[41] M. Weigand, A. Kemna, Multi-frequency electrical impedance tomography as a non-invasive tool to characterize and monitor crop root systems, Biogeosciences 14 (4) (2017) 921–939.
[42] Y. Li, et al., Imaging spatial-temporal distribution of moisture in intact maize ear, Measurement (2022), 111809.
[43] B. Kitchenham, O. Pearl Brereton, D. Budgen, M. Turner, J. Bailey, S. Linkman, Systematic literature reviews in software engineering – a systematic literature review, Inf. Software Technol. 51 (1) (2009) 7–15.
[44] T.K. Bera, J. Nagaraju, G. Lubineau, Electrical impedance spectroscopy (EIS)-based evaluation of biological tissue phantoms to study multifrequency electrical impedance tomography (Mf-EIT) systems, J. Visual 19 (4) (2016) 691–713.
[45] R.N. Deo, J.P. Cull, Spectral induced polarization techniques in soil corrosivity assessments, Geotech. Test J. 38 (6) (2015).
[46] Y. Ando, K. Mizutani, N. Wakatsuki, Electrical impedance analysis of potato tissues during drying, J. Food Eng. 121 (2014) 24–31.
[47] S. Anand, P. Jandial, R. Nersisson, A technical survey on hardware configurations for electrical impedance tomography systems, in: Presented at the 2021 Innovations in Power and Advanced Computing Technologies (i-PACT), 2021.
[48] Y. Wu, F.F. Hanzaee, D. Jiang, R.H. Bayford, A. Demosthenous, Electrical impedance tomography for biomedical applications: circuits and systems review, IEEE Open J. Circuits Syst. 2 (2021) 380–397.

[49] N. Polydorides, W. Lionheart, A Matlab toolkit for three-dimensional electrical impedance tomography: a contribution to the Electrical Impedance and Diffuse Optical Reconstruction Software project, Meas. Sci. Technol. 13 (12) (2002) 1871–1883.
[50] C. Dimas, K. Asimakopoulos, P.P. Sotiriadis, A highly tunable dynamic thoracic model for Electrical Impedance Tomography, in: Presented at the 2020 IEEE 20th International Conference on Bioinformatics and Bioengineering (BIBE), 2020.
[51] M.W. Sifuna, M.R. Baidillah, D. Kawashima, P.N. Darma, E.O. Odari, M. Takei, Determination of sensitive frequency margin for aggregated protein concentration quantification by fd-electrical impedance tomography, Measurement 186 (2021).
[52] Q.X. Pan, Y. Li, N. Wang, P.F. Zhao, L. Huang, Z.Y. Wang, Variational mode decomposition-based synchronous multi-frequency electrical impedance tomography, Inf. Technol. Control 51 (3) (2022) 446–466.
[53] N. Tarabi, H. Mousazadeh, A. Jafari, J. Taghizadeh-Tameh, A. Kiapey, Experimental evaluation of some current injection-voltage reading patterns in electrical impedance tomography (EIT) and comparison to simulation results - case study: large scales, Flow Meas. Instrum. 83 (2022).
[54] P.F. Zhao, et al., Evaluation of electrical impedance tomography sensor using internal-external electrodes for small-scale cylindrical root zones, Measurement 192 (2022).
[55] A. Adler, W.R. Lionheart, Uses and abuses of EIDORS: an extensible software base for EIT, Physiol. Meas. 27 (5) (2006) S25–S42.
[56] B. Liu, et al., pyEIT: a python based framework for Electrical Impedance Tomography, SoftwareX 7 (2018) 304–308.
[57] A. Coxson, et al., Machine learning enhanced electrical impedance tomography for 2D materials, Inverse Probl. 38 (8) (2022).
[58] T. Rymarczyk, G. Klosowski, E. Kozlowski, P. Tchorzewski, Comparison of selected machine learning algorithms for industrial electrical tomography, Sensors (Basel) 19 (7) (2019).
[59] P.N. Darma, M. Takei, High-speed and accurate meat composition imaging by mechanically-flexible electrical impedance tomography with k-nearest neighbor and fuzzy k-means machine learning approaches, IEEE Access 9 (2021) 38792–38801.
[60] Z. Chen, Y. Yang, P.-O. Bagnaninchi, Hybrid learning-based cell aggregate imaging with miniature electrical impedance tomography, IEEE Trans. Instrum. Meas. 70 (2021) 1–10.
[61] S.J. Hamilton, A. Hauptmann, Deep D-bar: real-time electrical impedance tomography imaging with deep neural networks, IEEE Trans. Med. Imag. 37 (10) (2018) 2367–2377.
[62] Z. Chen, Y. Yang, J. Jia, P. Bagnaninchi, Deep learning based cell imaging with electrical impedance tomography, in: 2020 IEEE International Instrumentation and Measurement Technology Conference (I2MTC), IEEE, 2020, pp. 1–6.
[63] Y. Fan, L. Ying, Solving electrical impedance tomography with deep learning, J. Comput. Phys. 404 (2020).
[64] Z. Chen, J. Xiang, P. Bagnaninchi, Y. Yang, MMV-net: a multiple measurement vector network for multi-frequency electrical impedance tomography, IEEE Transact. Neural Networks Learn. Syst. (2021), https://doi.org/10.1109/TNNLS.2022.3154108.
[65] Y. Zhang, C. Harrison, Tomo: wearable, low-cost electrical impedance tomography for hand gesture recognition, in: Proceedings of the 28th Annual ACM Symposium on User Interface Software & Technology, 2015, pp. 167–173.
[66] E. Dunne, A. Santorelli, B. McGinley, G. Leader, M. O'Halloran, E. Porter, Image-based classification of bladder state using electrical impedance tomography, Physiol. Meas. 39 (12) (2018), 124001.
[67] B. McDermott, A. Elahi, A. Santorelli, M. O'Halloran, J. Avery, E. Porter, Multi-frequency symmetry difference electrical impedance tomography with machine learning for human stroke diagnosis, Physiol. Meas. 41 (7) (2020), 075010.
[68] D. Pessoa, et al., Classification of electrical impedance tomography data using machine learning, in: Annu Int Conf IEEE Eng Med Biol Soc, vol. 2021, 2021, pp. 349–353.
[69] Z. Husain, N.A. Madjid, P. Liatsis, Tactile sensing using machine learning-driven electrical impedance tomography, IEEE Sensor. J. 21 (10) (2021) 11628–11642.
[70] T.A. Khan, S.H. Ling, Review on electrical impedance tomography: artificial intelligence methods and its applications, Algorithms 12 (5) (2019).
[71] T.I. Oh, H. Wi, D.Y. Kim, P.J. Yoo, E.J. Woo, A fully parallel multi-frequency EIT system with flexible electrode configuration: KHU Mark2, Physiol. Meas. 32 (7) (2011) 835–849.
[72] Y. Yang, An Advanced Digital Electrical Impedance Tomography System for Biomedical Imaging, The University of Edinburgh, 2018. Ph.D.
[73] T.I. Oh, K.H. Lee, S.M. Kim, H. Koo, E.J. Woo, D. Holder, Calibration methods for a multi-channel multi-frequency EIT system, Physiol. Meas. 28 (10) (2007) 1175–1188.
[74] J. Lee, U. Ha, H.J. Yoo, 30-fps SNR equalized electrical impedance tomography IC with fast-settle filter and adaptive current control for lung monitoring, in: 2016 IEEE International Symposium on Circuits and Systems (ISCAS), IEEE, 2016, pp. 109–112.
[75] C. Dimas, P. Tsampas, N. Ouzounoglou, P.P. Sotiriadis, Development of a modular 64-electrodes electrical impedance tomography system, in: 2017 6th International Conference on Modern Circuits and Systems Technologies (MOCAST), 2017.
[76] M. San-Pablo-Juárez, E. Morales-Sánchez, F. Ireta-Moreno, R. Ávalos-Zúñiga, J.-J. González-Barbosa, Design of an HMI electrical impedance tomography system based on off-the-shelf components, in: 2016 International Conference on Electronics, Communications and Computers (CONIELECOMP), IEEE, 2016, pp. 101–105.
[77] H. McCann, S.T. Ahsan, J.L. Davidson, R.L. Robinson, P. Wright, C.J. Pomfrett, A portable instrument for high-speed brain function imaging: FEITER, in: 2011 Annual International Conference of the IEEE Engineering in Medicine and Biology Society, vol. 2011, 2011, pp. 7029–7032.
[78] Y. Yang, J. Jia, A multi-frequency electrical impedance tomography system for real-time 2D and 3D imaging, Rev. Sci. Instrum. 88 (8) (2017), 085110.
[79] M.R. Baidillah, Z. Gao, A.-A.S. Iman, M. Takei, Adaptive noise cancellation algorithms implemented onto FPGA-based electrical impedance tomography system, Electr. Sci. Eng. 1 (2) (2019).
[80] T.I. Oh, E.J. Woo, D. Holder, Multi-frequency EIT system with radially symmetric architecture: KHU Mark1, Physiol. Meas. 28 (7) (2007) S183–S196.
[81] H. Wi, E.J. Woo, Design of KHU mark2 multi-frequency EIT System, in: Proc. Int. Conf. On Biomedical Applications of Electrical Impedance Tomography (Mancheter), 2009.
[82] H. Wi, H. Sohal, A.L. McEwan, E.J. Woo, T.I. Oh, Multi-frequency electrical impedance tomography system with automatic self-calibration for long-term monitoring, IEEE Trans. Biomed. Circuits Syst. 8 (1) (2014) 119–128.
[83] H. Tran, V. Pham, T. Le, H. Yoon, J. Kim, Signal processing to improve the speed and accuracy of electrical impedance tomography imaging, in: Presented at the Nano-, Bio-, Info-Tech Sensors and Wearable Systems, 2021.
[84] Z. Xu, et al., Development of a portable electrical impedance tomography system for biomedical applications, IEEE Sensor. J. 18 (19) (2018) 8117–8124.
[85] B. McDermott, M. O'Halloran, J. Avery, E. Porter, Bi-frequency symmetry difference EIT-feasibility and limitations of application to stroke diagnosis, IEEE J. Biomed. Health Inf. 24 (8) (2020) 2407–2419.
[86] L. Yang, et al., The frequency spectral properties of electrode-skin contact impedance on human head and its frequency-dependent effects on frequency-difference EIT in stroke detection from 10Hz to 1MHz, PLoS One 12 (1) (2017), e0170563.
[87] J. Xia, B. Liu, X. Shi, F. Feng, X. Dong, Study on howland circuits for low power electrical impedance tomography systems, in: 2018 11th International Congress on Image and Signal Processing, BioMedical Engineering and Informatics (CISP-BMEI), 2018.
[88] L. Constantinou, I.F. Triantis, R. Bayford, A. Demosthenous, High-power CMOS current driver with accurate transconductance for electrical impedance tomography, IEEE Trans. Biomed. Circuits Syst. 8 (4) (2014) 575–583.
[89] O.R. Shishvan, A. Abdelwahab, G.J. Saulnier, Practical implementation of a novel output impedance measurement technique for EIT system while attached to a load, in: 2021 43rd Annual International Conference of the IEEE Engineering in Medicine & Biology Society (EMBC), vol. 2021, 2021, pp. 3952–3956.
[90] J. Jang, H.-J. Yoo, Low power and accurate current driver IC for electrical impedance tomography applications, J. Semiconduct. Technol. Sci. 19 (1) (2019) 109–115.
[91] D.Y. Kim, H. Wi, P.J. Yoo, T.I. Oh, E.J. Woo, Performance evaluation of KHU Mark2 parallel multi-frequency EIT system, J. Phys. Conf. 224 (2010).
[92] H. Sohal, H. Wi, A.L. McEwan, E.J. Woo, T.I. Oh, Electrical impedance imaging system using FPGAs for flexibility and interoperability, Biomed. Eng. Online 13 (2014) 126.

[93] H. Hong, M. Rahal, A. Demosthenous, R.H. Bayford, Comparison of a new integrated current source with the modified Howland circuit for EIT applications, Physiol. Meas. 30 (10) (2009) 999–1007.
[94] W. Yu, J. Dai, P. Langlois, R. Bayford, A. Demosthenous, A CMOS current driver with built-in common-mode signal reduction capability for EIT, in: ESSCIRC 2017 - 43rd IEEE European Solid State Circuits Conference (ESSCIRC), 2017.
[95] J. Jang, M. Kim, J. Bae, H.J. Yoo, A 2.79-mW 0.5%-THD CMOS current driver IC for portable electrical impedance tomography system, in: Solid-state Circuits Conference, 2017.
[96] W. Li, et al., Fast high-precision electrical impedance tomography system for real-time perfusion imaging, IEEE Access 7 (2019) 61570–61580.
[97] L. Fabrizi, A. McEwan, T. Oh, E.J. Woo, D.S. Holder, An electrode addressing protocol for imaging brain function with electrical impedance tomography using a 16-channel semi-parallel system, Physiol. Meas. 30 (6) (2009) S85–S101.
[98] T. Dowrick, C. Blochet, N. Chaulet, D. Holder, A Custom EIT System Based on Off-The-Shelf Equipment, 2014.
[99] Y. Wu, D. Jiang, A. Bardill, S. de Gelidi, R. Bayford, A. Demosthenous, A high frame rate wearable EIT system using active electrode ASICs for lung respiration and heart rate monitoring, IEEE Trans. Circuits Syst. I: Regul. Pap. 65 (11) (2018) 3810–3820.
[100] S. Hong, J. Lee, J. Bae, H.J. Yoo, A 10.4 mW electrical impedance tomography SoC for portable real-time lung ventilation monitoring system, IEEE J. Solid State Circ. 50 (11) (2015) 2501–2512.
[101] S. Russo, S. Nefti-Meziani, N. Carbonaro, A. Tognetti, Development of a high-speed current injection and voltage measurement system for electrical impedance tomography-based stretchable sensors, Technologies 5 (3) (2017).
[102] S. Xu, et al., Performance evaluation of five types of Ag/AgCl bio-electrodes for cerebral electrical impedance tomography, Ann. Biomed. Eng. 39 (7) (2011) 2059–2067.
[103] H. Wi, T.I. Oh, S. Yoon, K.J. Kim, E.J. Woo, Human interface design using Button-type PEDOT electrode array in EIT, J. Phys. Conf. 224 (2010).
[104] Y. Yang, J. Jia, S. Smith, N. Jamil, W. Gamal, P.-O. Bagnaninchi, A miniature electrical impedance tomography sensor and 3-D image reconstruction for cell imaging, IEEE Sensor. J. 17 (2) (2017) 514–523.
[105] K.F. Morcelles, P. Bertemes-Filho, Hardware for cell culture electrical impedance tomography: a critical review, Rev. Sci. Instrum. 92 (10) (2021), 104704.
[106] N. Jamil, S. Smith, Y. Yang, J. Jia, P. Bagnaninchi, E. Gonzalez-Fernandez, Design and fabrication of microelectrodes for electrical impedance tomography of cell spheroids, in: Presented at the 2016 IEEE EMBS Conference on Biomedical Engineering and Sciences (IECBES), 2016.
[107] H. Kwon, A.L. McEwan, T.I. Oh, A. Farooq, E.J. Woo, J.K. Seo, A local region of interest imaging method for electrical impedance tomography with internal electrodes, Comput. Math. Methods Med. (2013) (2013), 964918.
[108] Y. Wu, D. Jiang, A. Bardill, S.D. Gelidi, R. Bayford, A. Demosthenous, Live demonstration: a wearable torso shape detection belt for lung respiration monitoring, in: 2019 IEEE International Symposium on Circuits and Systems (ISCAS), 2019.
[109] J. Avery, Improving Electrical Impedance Tomography of Brain Function with a Novel Servo-Controlled Electrode Helmet, UCL (University College London), 2015.
[110] K. Sakai, P.N. Darma, P.A. Sejati, R. Wicaksono, H. Hayashi, M. Takei, Gastric functional monitoring by gastric electrical impedance tomography (gEIT) suit with dual-step fuzzy clustering, Sci. Rep. 13 (1) (2023) 514.
[111] P.O. Gaggero, A. Adler, J. Brunner, P. Seitz, Electrical impedance tomography system based on active electrodes, Physiol. Meas. 33 (5) (May 2012) 831–847.
[112] Y. Wu, P. Langlois, R. Bayford, A. Demosthenous, Design of a CMOS active electrode IC for wearable electrical impedance tomography systems, in: IEEE International Symposium on Circuits & Systems, 2016.
[113] Y. Wu, D. Jiang, A. Bardill, R. Bayford, A. Demosthenous, A 122 fps, 1 MHz bandwidth multi-frequency wearable EIT belt featuring novel active electrode architecture for neonatal thorax vital sign monitoring, IEEE Trans. Biomed. Circuits Syst. 13 (5) (Oct 2019) 927–937.
[114] J. Lee, U. Ha, H.J. Yoo, 0.025 mJ/image fast-scan and SNR enhanced electrical impedance tomography IC for lung ventilation monitoring, J. Semiconduct. Technol. Sci. 17 (6) (2017) 920–926.
[115] W. Mi, M. Yixin, N. Holliday, D. Yunfeng, R.A. Williams, G. Lucas, A high-performance EIT system, IEEE Sensor. J. 5 (2) (2005) 289–299.
[116] Y. Xu, Z. Yan, B. Han, F. Dong, An FPGA-based multifrequency EIT system with reference signal measurement, IEEE Trans. Instrum. Meas. 70 (2021) 1–10.
[117] W. Yu, J. Dai, J. Duan, L. Xiao, A. Demosthenous, Towards a high accuracy wearable hand gesture recognition system using EIT, in: 2018 IEEE International Symposium on Circuits and Systems (ISCAS), 2018.
[118] X. Shi, et al., High-precision electrical impedance tomography data acquisition system for brain imaging, IEEE Sensor. J. 18 (14) (2018) 5974–5984.
[119] Y. Ma, et al., A new modular semi-parallel EIT system for medical application, Biomed. Signal Process Control 39 (2018) 416–423.
[120] M. Darnajou, A. Dupre, C. Dang, G. Ricciardi, S. Bourennane, C. Bellis, On the implementation of simultaneous multi-frequency excitations and measurements for electrical impedance tomography, Sensors (Basel) 19 (17) (2019).
[121] C. Dimas, N. Uzunoglu, P.P. Sotiriadis, A parametric EIT system Spice simulation with phantom equivalent circuits, Technologies 8 (1) (2020).
[122] C. Dimas, V. Alimisis, I. Georgakopoulos, N. Voudoukis, N. Uzunoglu, P.P. Sotiriadis, Evaluation of thoracic equivalent multiport circuits using an electrical impedance tomography hardware simulation interface, Technologies 9 (3) (2021).
[123] H. Wu, Y. Yang, P.-O. Bagnaninchi, J. Jia, Calibrated frequency-difference electrical impedance tomography for 3D tissue culture monitoring, IEEE Sensor. J. 19 (18) (2019) 7813–7821.
[124] Y.C. Teng, K.M. Odame, A 10 MHz 85 dB dynamic range instrumentation amplifier for electrical impedance tomography, in: 2014 IEEE Biomedical Circuits and Systems Conference (BioCAS) Proceedings, IEEE, 2014, pp. 632–635.
[125] X. Lu, S. Sun, K. Liu, J. Sun, L. Xu, Development of a wearable gesture recognition system based on two-terminal electrical impedance tomography, IEEE J. Biomed. Health Inf. 26 (6) (2022) 2515–2523.